The Astrophysical Journal, 968:82 (7pp), 2024 June 20 https://doi.org/10.3847/1538-4357/ad479f

Energetic Electrons Observed Inside Magnetic Holes in the Magnetotail

Yi Xie[1,2,3], Rongsheng Wang[1,2,3], Xinmin Li[1,2,3], Shimou Wang[1,2,3], Keming Fan[1,2,3], Quanming Lu[1,2,3], Xinliang Gao[1,2,3], and San Lu[1,2,3]
[1] Deep Space Exploration Laboratory, School of Earth and Space Sciences, University of Science and Technology of China, Hefei, People's Republic of China; rswan@ustc.edu.cn
[2] CAS Center for Excellence in Comparative Planetology, CAS Key Laboratory of Geospace Environment, Anhui Mengcheng National Geophysical Observatory, University of Science and Technology of China, Hefei, People's Republic of China
[3] Collaborative Innovation Center of Astronautical Science and Technology, Harbin, People's Republic of China
Received 2024 February 1; revised 2024 April 11; accepted 2024 May 2; published 2024 June 13

Abstract

Magnetic holes, characterized as magnetic field depressions, have been widely observed in space plasma. Two large-scale magnetic holes, MH1 and MH2, were reported in this paper and the energetic electrons up to 100 keV were detected for the first time inside both holes. The two holes showed many similar features, comparable spatial scale, temperature and total pressure increase, and energetic electrons up to 100 keV with a power-law distribution inside them. On the other hand, distinct features were also found between these two holes. A potential ion flow vortex was detected inside the MH1 and an ion-scale magnetic structure was observed in its core region. The electron flux enhancements were associated with this ion-scale structure and the energetic electrons were nonadiabatic around the ion-scale structure inside MH1, while the energetic electrons were adiabatic inside the MH2. The mirror-mode instability was unstable around MH1 while stable around MH2, which suggested that the two holes might be in a different phase of the mirror-mode instability. The observations suggested that the electrons could be significantly accelerated inside magnetic holes in the different phases.

Unified Astronomy Thesaurus concepts: Magnetic fields (994); Solar magnetic reconnection (1504); Planetary magnetospheres (997)

1. Introduction

Magnetic holes (MHs), known as magnetic decreases (Tsurutani & Ho 1999) or magnetic depressions (Fränz et al. 2000), are magnetic structures with intense depression in the magnitude of the magnetic field. They were first reported by Turner et al. (1977) in the solar wind, and then widely observed in the Earth's and other planets' magnetosheath (Tsurutani et al. 1982; Lucek et al. 1999; Joy et al. 2006; Soucek et al. 2008; Balikhin et al. 2009; Huang et al. 2017b; Yao et al. 2017), the cusp region (Shi et al. 2009), planetary magnetotail (Ge et al. 2011; Sun et al. 2012), and even cometary cones (Russell et al. 1987). Magnetic holes have a wide range of spatial scales from several electron gyroradius (ρ_e) to thousands of proton gyroradius (ρ_i) (Winterhalter et al. 1994; Sperveslage et al. 2000). Generally, magnetic holes are thought to be generated by the mirror-mode instability (Southwood & Kivelson 1993; Gary & Karimabadi 2006; Pokhotelov et al. 2013).

Magnetic holes are common in the magnetosphere. However, the physics inside kinetic-scale magnetic holes was only revealed recently with the high-resolution spacecraft data (Huang et al. 2017b; Yao et al. 2017; Huang et al. 2018; Shustov et al. 2019; Zhong et al. 2019; Liu et al. 2020; Wang et al. 2022; Zhong et al. 2022). Since the electrons are trapped inside magnetic holes, they display pancake distribution and form the electron vortex inside the holes (Haynes et al. 2015; Roytershteyn et al. 2015). A statistical analysis of the kinetic-scale magnetic holes showed that the density was enhanced, the electron perpendicular temperature increased and the parallel electron temperature was moderately decreased (Huang et al. 2017a). Furthermore, an ion-scale magnetic hole was investigated in detail and an ion vortex was detected within it (Yao et al. 2023). This ion flow vortex was thought to be caused by diamagnetic drift. The axial magnetic field was reversed near the vortex center, consistent with the ring-shaped currents carried by the ion diamagnetic motion. The electron cyclotron harmonic waves (Zhang et al. 2017), electrostatic solitary waves (Yao et al. 2019), and whistler waves (Huang et al. 2018; Yao et al. 2019, 2021) were detected in the holes, and they could be generated locally inside the holes (Zhima et al. 2015; Huang et al. 2018; Yao et al. 2019). Although the thermal electron distribution feature has been studied, the energetic electrons have never been detected inside the holes.

In this paper, we report direct evidence of energetic electrons in two MHD-scale magnetic holes in the magnetotail. Based on the electron distributions, we propose that the electrons were trapped inside the holes and were directly accelerated to ~100 keV.

2. Spacecraft Database

The data from the Magnetospheric Multiple Scale (MMS) mission are used in the study (Burch et al. 2016). The MMS spacecraft consists of four satellites. Magnetic field data are measured by the Fluxgate Magnetometer (Russell et al. 2016) with a time resolution of 1/16 s (survey mode). Plasma data are taken from the Fast Plasma Instrument (FPI; Pollock et al. 2016) with a time resolution of 4.5 s. All-sky distributions of energetic electrons (~45 to ~650 keV) are measured by the Fly's Eye Energetic Particle Spectrometer (FEEPS; Blake et al. 2016). Due to the similar observations by the four MMS spacecraft, only the data from MMS1 are present. The coordinate system of the Geocentric Solar Ecliptic (GSE) coordinates is used throughout this paper.

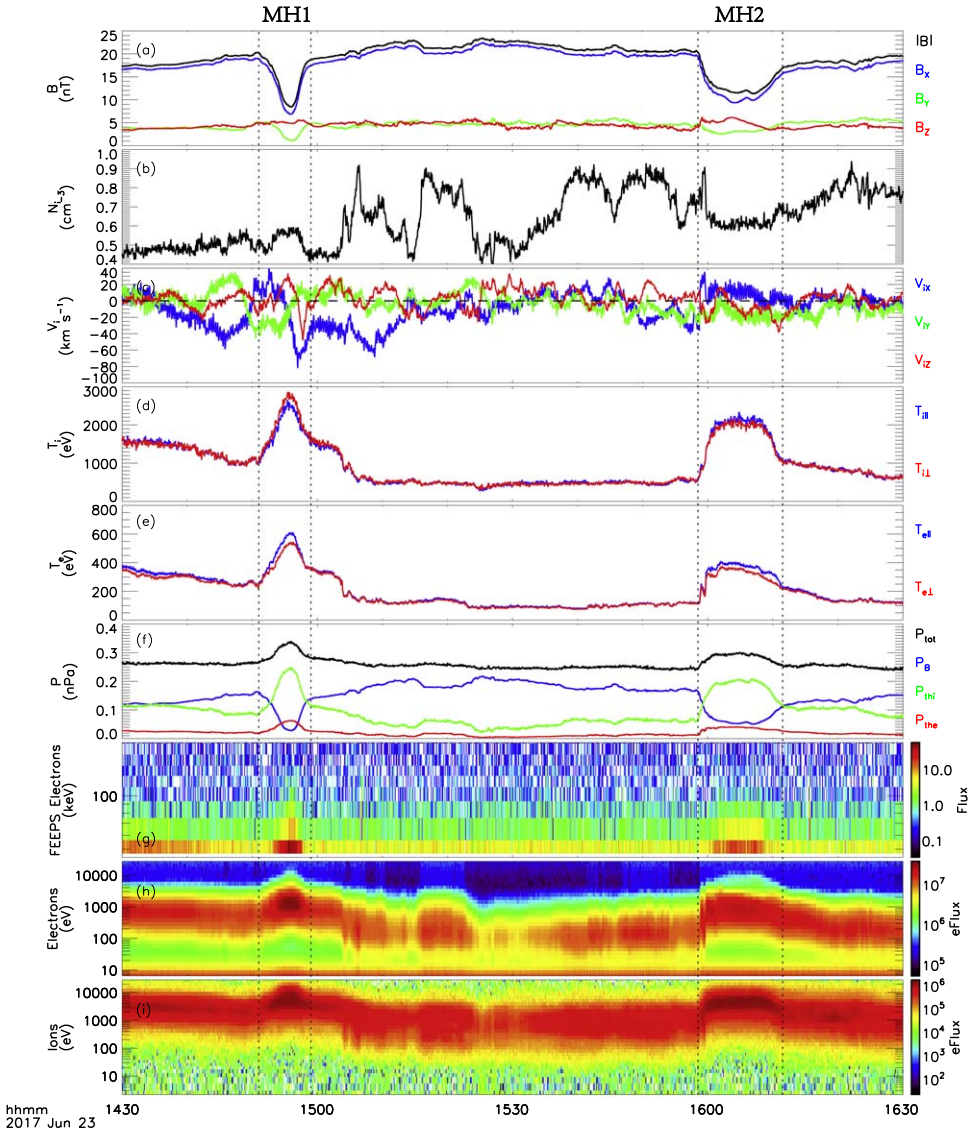

Figure 1. Overview of MMS1 measurements from 14:30 UT to 16:30 UT on 2017 June 23 in the magnetotail. Panels from the top to the bottom are (a) three components and magnitude of the magnetic fields, (b) ion number density, (c) ion flow velocity, (d) perpendicular and parallel ion temperature, (e) perpendicular and parallel electron temperature, (f) total pressure, electron thermal pressure, ion thermal pressure, and magnetic pressure, (g) and (h) omnidirectional electron energy spectrum measured by Fly's Eye Energetic Particle Spectrometer (FEEPS) and Fast Plasma Investigation (FPI), and (i) omnidirectional ion energy spectrum measured by FPI. The vertical dashed black lines indicate the boundary of the two magnetic holes.

3. Observation and Analysis

3.1. Event Overview

Figure 1 presents an overview of MMS1 measurements from 14:30 UT to 16:30 UT on 2017 June 23 at (−17.9, −8.8, 5.4) Re in the magnetotail. During the 2 hr interval, the spacecraft encountered two intense depressions in the magnetic strength $|\boldsymbol{B}|$ (black line in Figure 1(a)) in the GSE coordinate system. The first $|\boldsymbol{B}|$ depression was observed between 14:51:00 UT and 14:59:00 UT. The second was observed between 15:58:30 UT and 16:11:30 UT. The two magnetic depressions were marked by two vertical dashed black lines, and named as magnetic hole 1 and magnetic hole 2 (MH1 and MH2).

The ion number density (Figure 1(b)) showed no obvious increase inside MH1 while a slight decrease inside MH2 relative to the background number density. The ion bulk velocity (Figure 1(c)) showed complicated variation inside both depressions and the flow speed was higher in MH1 than that in MH2. There was a background bulk flow, mainly in the x-component around MH1 (~ -27.9 km s^{-1}) and in the y-direction around MH2 (-10.8 km s^{-1}). All three components of the ion flow changed sign inside MH1, which indicates that there could be an ion flow vortex. In contrast, all three components of ion flows changed sign sharply near the leading edge of MH2 (the left vertical dashed line around MH2), which may be caused by the interaction of the hole with the background plasma. The ion temperature (Figure 1(d)) and electron temperature (Figure 1(e)) enhanced sharply inside both magnetic holes. The electron temperature anisotropy was clear inside both holes, and the parallel temperature was larger than the perpendicular component. On the contrary, the ion temperature anisotropy was not evident inside both depressions.

The magnetic depression in the magnetotail can be caused by the partial crossing of the magnetotail current sheet. As the spacecraft was approaching the current sheet center during a partial crossing, both the magnetic depression and the plasma

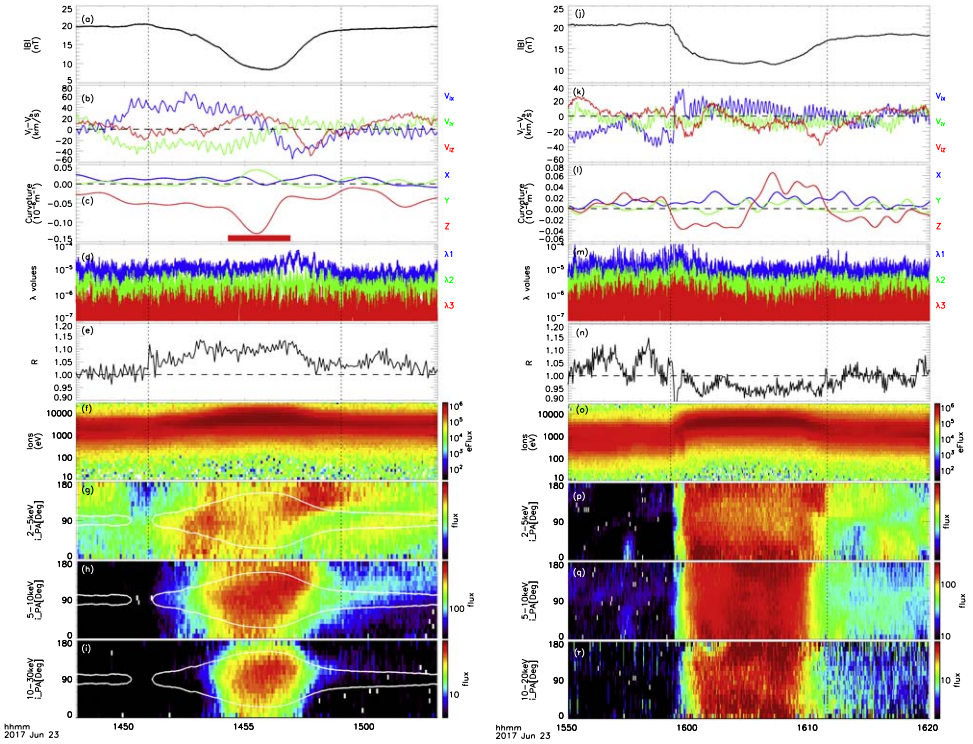

Figure 2. Zoom-in plot of the detailed properties inside MH1 (a–j) and MH2 (k–t). (a) Magnitude, (b) ion bulk flow velocity in the magnetic hole frame, (c) magnetic field curvature, (d) eigenvalues $\lambda1$, $\lambda2$, and $\lambda3$ in MDD method, (e) ion mirror instability $R = \frac{T_{i,\perp}}{T_{i,\mathrm{P}}} - \frac{1}{\beta_{i,\perp}}$, (f) omnidirectional thermal ion fluxes, (g) 2–5 keV, (h) 5–10 keV, and (i) 10–30 keV ions pitch angle distributions (PADs). (j–r) are the same format as (a)–(i) for MH2. The vertical dashed black lines indicate the boundary of the two magnetic holes as shown in Figure 1. The white curves indicate the ion loss cones determined by the ambient $|\boldsymbol{B}| = 20$ nT.

density enhancements should be observed simultaneously. However, the number density did not increase in both magnetic depressions, and the density in the MH2 even declined obviously. Therefore, it is concluded that both magnetic depressions were caused by magnetic holes rather than partial current sheet crossings.

The total pressure (Figure 1(f)) was enhanced due to the significant increases in the plasma pressure within both holes. It indicates that the two magnetic structures were varying and were not in the steady state. The thermal electron and ion differential energy fluxes are displayed in Figure 1(h) and Figure 1(i), respectively. The electron ($\sim$5– $\sim$ 10 keV) and ion ($\sim$2– $\sim$ 30 keV) fluxes were significantly enhanced. Namely, the electrons and ions were trapped inside the holes. Furthermore, the fluxes of electrons with energy up to 100 keV (Figure 1(g)) were detected as well inside both holes and the high energy electron flux enhancement mainly concentrated on the center of the hole (minimum value of $|\boldsymbol{B}|$). It means that the electrons could be directly accelerated.

3.2. Observations inside the Holes

Figure 2 presents the detailed observations of the two magnetic holes. Figures 2(a) and (j) display the field magnitude in MH1 and MH2, respectively. Since the MMS mission consists of four identical satellites forming a three-dimensional structure, we can calculate the field curvature by the equation $\boldsymbol{b}\cdot\boldsymbol{\nabla b}$, where $\boldsymbol{b} = \frac{\boldsymbol{B}}{|\boldsymbol{b}|}$ and $\boldsymbol{B}$ is the magnetic field vector. To reduce the effect of the high-frequency fluctuations, the low-pass filter was performed on magnetic field data with a cutoff frequency of 0.01 Hz, and the magnetic field curvature vector is displayed in Figures 2(c) and (l). The z-component of magnetic field curvature was dominant and had a negative peak at the local minimum (at $\sim$14:56 UT) of $|\boldsymbol{B}|$ inside MH1 (red trace in Figure 2(c)). Thus, the spacecraft should just cross one side of the hole, as illustrated in Figure 3(a). The sharp decrease of the z-component of magnetic field curvature (red bar at the bottom of Figure 2(c)) means that there was a small-scale magnetic structure at the hole core region and its spatial scale was estimated later.

In contrast, the magnetic field curvature vector inside the MH2 is dominated by the z-component as well (Figure 2(l)). However, the z-component changed sign from negative to positive near the center of the hole (minimum value of $|\boldsymbol{B}|$ in Figure 2(j)). Therefore, the spacecraft passed through the hole from one half with the negative curvature in the z-component to the other half with the positive curvature in the z-component (the red curve in Figure 3(b)). The minimum directional derivative (MDD) method (Shi et al. 2005) was used further to determine the magnetic structure. The three eigenvalues fluctuated largely around both holes (Figures 2(d) and (m)), which indicates that the magnetic structures were intricate. At $\sim$14:57 UT, the eigenvalue $\lambda1$ was much bigger than the other two eigenvalues, which means that the magnetic structure tended to be one-dimensional at the local position. Simultaneously, the magnetic field gradient was also larger (Figure 2(a)). It indicates that the magnetic hole structures were varying while they were encountered by the spacecraft.

Assuming the holes were moving together with the background speed, the ion flows with respect to the magnetic structures can be obtained and shown in Figures 2(b) and (k). The ion bulk flows were quite different within these two holes. Inside the MH1, v_{ix} reversed at 14:56 UT from positive to negative. Given that the magnetic field was primarily in the

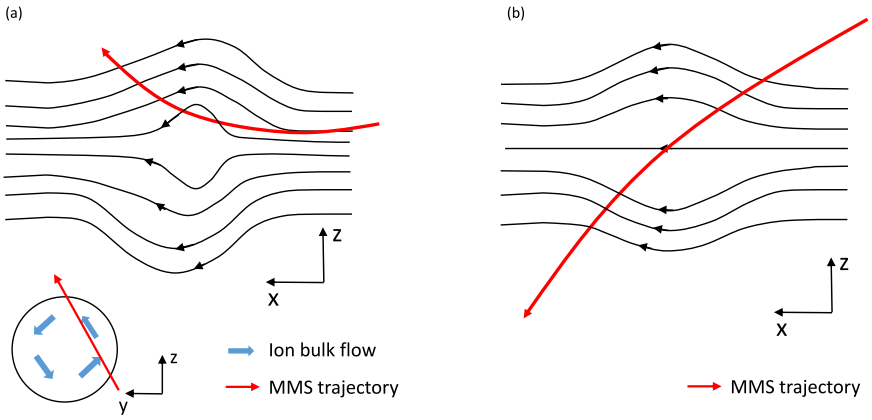

Figure 3. Schematic diagram of MH1(a) and MH2 (b). The black lines are magnetic field lines. The red line is the MMS trajectory. The blue arrows indicate the ion bulk flow.

x-component, v_{ix} was mainly along the magnetic field direction. The magnetized ions were bouncing between two mirror points and thus they were gathering toward the hole center (minimum of magnetic field). This could be the reason for the v_{ix} reversal inside the hole. The y- and z-component of ion flows v_{iy} and v_{iz} changed sign simultaneously at ~14:57 UT. It seems that there was an ion flow vortex in the y-z plane, as shown in the schematic at the bottom of Figure 3(a), consistent with previous observations where an ion flow vortex was observed inside the magnetic hole (Wang et al. 2021; Yao et al. 2023). On the other hand, the ion flow v_{ix} and v_{iz} sharply reversed at ~15:59 UT at the leading edge of the MH2 and then did not change significantly inside it. At the leading edge of MH2, the ion energy time spectrum (Figure 2(o)) showed a clear evolution. It indicates that there was a thin boundary therein.

Assuming the holes were moving constantly while they were encountered by the spacecraft, their sizes can be roughly estimated. The scale of MH1 was $-27.9\ \mathrm{km\ s^{-1}} \times 480\mathrm{s} = 13392\ \mathrm{km} \sim 59\ \rho_i$, where $\rho_i = 228\ \mathrm{km}$ was determined by the ambient $T_i =$ ~1000 eV and $|\boldsymbol{B}| = \sim 20$ nT. Considering that the MMS spacecraft did not cross MH1 completely, the actual size was larger than our estimate. For the small-scale structure at the core region of MH1, the duration was about 2 minutes and thus the total spatial scale was roughly estimated to be 15 ρ_i, an ion-scale magnetic structure. In the same way, the size of MH2 was estimated to be $10.8\ \mathrm{km\ s^{-1}} \times 13 \times 60\ \mathrm{s} = 8424\ \mathrm{km} \sim 37\ \rho_i$.

The magnetic holes are generally thought to be resulting from the ion mirror instability. The threshold condition of the ion mirror instability is $R = \frac{T_{i,\perp}}{T_{i,\mathrm{P}}} - \frac{1}{\beta_{i,\perp}} > 1$ (Southwood & Kivelson 1993). In the vicinity of the MH1, R was always larger than 1 (Figure 2(e)). It suggested that the ion mirror instability can be excited and lead to the generation of MH1. R was larger than 1 only prior to MH2 and then was ~0.9, slightly less than 1, within and after MH2. Namely, the R-value was near the threshold of the ion mirror instability. One potential explanation for this situation was that MH2 was also excited by the mirror instability but the ambient plasma environment was modified while it was encountered by the spacecraft.

The ion and electron differential energy fluxes are shown in Figures 1(g)–(i). The ion flux enhancements were observed inside both holes at a certain energy range of 1–30 keV (Figure 1(i)). The electron flux enhancements can be observed in the energy range of 700 eV–10 keV (Figure 1(h)). Furthermore, the energetic electron fluxes were significantly enhanced at energy up to 100 keV (Figure 1(g)) and the enhancements were concentrated on the locations with the minimum of $|\boldsymbol{B}|$. The ion pitch angle distributions (PADs) are shown in Figures 2(g)–(i) and Figures 2(p)–(r). The ions parallel to the magnetic field can be observed in the left half of MH1 (~prior to 14:56 UT) while the ions antiparallel to the magnetic field were detected in the right half. Moreover, the trapped ions at ~90° can be clearly observed in the energy range of 2–30 keV (Figures 2(g)–(i)) around the ion-scale structure of the MH1. Inside the MH2, the ion flux increase was also evident (Figure 2(o)). The ions parallel and antiparallel to the magnetic field were detected in the energy range of 2–5 keV (Figure 2(p)). The PADs in the energy range of 5–20 keV (Figures 2(q)–(r)) displayed a similar isotropic feature.

The thermal and energetic electrons associated with the two holes are presented in Figure 4. The left and right columns corresponded to MH1 and MH2, respectively. The adiabaticity parameters $\kappa^2 = \frac{R_c}{\rho}$ for electrons inside MH1 and MH2 are calculated in Figures 4(b) and (i), where $R_c = \frac{1}{|\boldsymbol{b}\cdot\nabla\boldsymbol{b}|}(\boldsymbol{b} = \frac{\boldsymbol{B}}{|\boldsymbol{B}|})$ is the magnetic field curvature radius and ρ is the electron gyroradius. The three color lines represent the energies of electrons with different perpendicular velocities. κ^2 values usually denote the particle motion in the magnetized plasma (Buchner & Zelenyi 1989). The electron curvature scattering occurs while the κ^2 values are below 25 ($\kappa^2 = 25$ denoted by the horizontal dashed line in Figures 4(b) and (i)), and the electron orbits are chaotic while the κ^2 values are below 10 ($\kappa^2 = 10$ denoted by the horizontal dotted line in Figures 4(b) and (i)). Inside MH1, the electrons with energy lower than 30 keV were adiabatic because their κ^2 values were above 25. The electrons with energy larger than 30 keV were adiabatic as well but became nonadiabatic around the ion-scale structure in the core region of MH1. As for the electrons from 1 keV to 90 keV inside MH2, they were basically adiabatic since the κ^2 values were larger than 25.

The PAD of the electrons from 0.2 to 90 keV can be found in Figures 4(e)–(g) (MH1) and Figures 4(l)–(n) (MH2). Inside MH1, the low energy electrons (0.2–3 keV; Figure 4(e)) displayed field-aligned bidirectional distribution. As the energy of the electrons increased, the flux enhancement at ~90° became evident (Figures 4(f) and (g)) in addition to the field-aligned flux increase. A similar electron PAD was observed also from 0.2 to 90 keV inside the MH2 (Figures 4(l)–(n)). The white curves in Figures 4(e)–(g) and Figures 4(l)–(n) indicated the electron loss cones determined by the ambient $|\boldsymbol{B}| = 20$ nT.

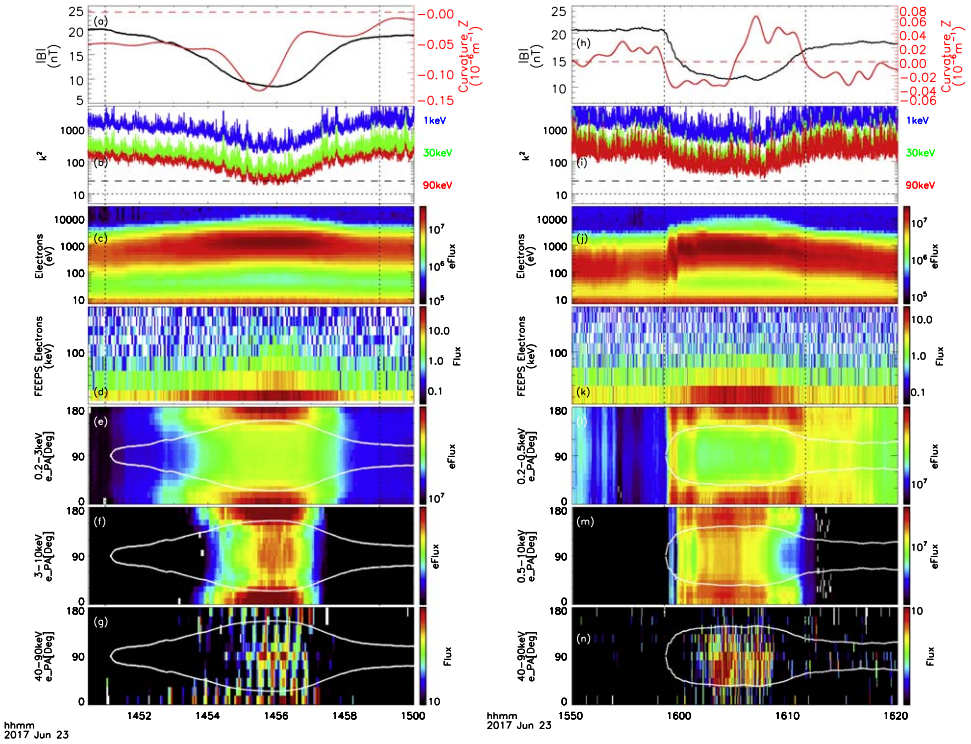

Figure 4. The electron pitch angle distributions (PADs) inside MH1 (a–g) and MH2 (h–n). (a) Magnitude and z-component of magnetic field curvature, (b) the adiabaticity parameter κ, (c) and (d) omnidirectional thermal electron fluxes measured by FPI and energetic electron fluxes measured by FEEPS, (e) 0.2–3 keV, (f) 3–10 keV, and (g) 40–90 keV electron PADs for MH1. (h–k) are in the same format as (a–d) but for MH2. (l) 0.2–0.5 keV, (m) 0.5–10 keV, and (n) 40–90 keV electron PADs for MH2. The vertical dashed black lines indicate the boundary of the two magnetic holes as shown in Figure 1. The white curves indicate the electron loss cones determined by the ambient $|\boldsymbol{B}| = 20$ nT.

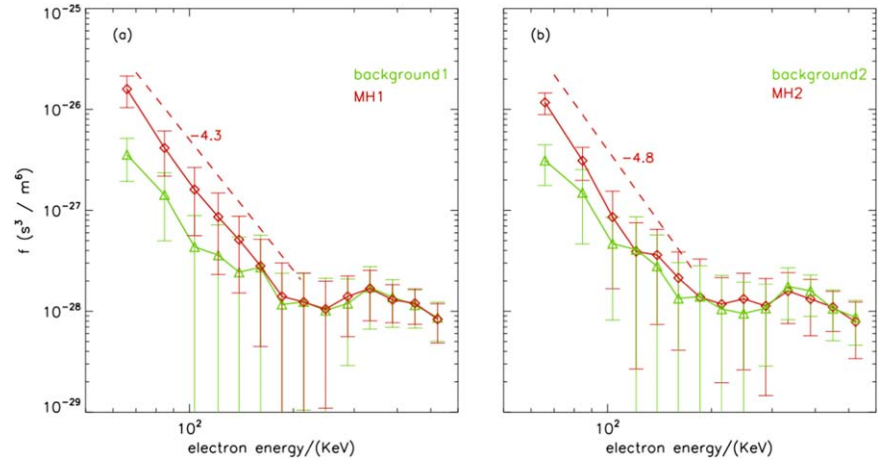

Figure 5. Electron energy spectra of MH1 (a) and MH2 (b) for FEEPS data. Empty triangles and squares with error bars are measured data by FEEPS. (a) The energy spectra of the background near MH1 (green line, from 14:40:00 UT to 14:42:00 UT) and inside MH1 (red line, from 14:55:00 UT to 14:57:00 UT). The red dashed line shows the power-law fitting between 50 and 200 keV with an index of −4.3 for the PSD for MH1. (b) The energy spectra of the background near MH2 (green line, from 16:04:00 UT to 16:06:00 UT) and inside MH2 (red line, from 16:20:00 UT to 16:22:00 UT). The red dashed line shows the power-law fitting between 50 and 200 keV with an index of −4.8 for the PSD for MH2.

The flux enhancement of the higher energy electrons (40–90 keV) was concentrated within the upper and lower white curves, suggesting that these energetic electrons were trapped inside the holes. The electron energy spectra observed outside (green line, from 14:40:00 UT to 14:42:00 UT) and inside MH1 (red line, from 14:55:00 UT to 14:57:00 UT) were displayed in Figure 5(a). The energetic electrons inside MH1 showed a power-law distribution with an index of 4.3 between 50 and 200 keV, indicating that the electrons had been accelerated substantially. The electron energy spectra outside (green line, from 16:04:00 UT to 16:06:00 UT) and inside MH2 (red line, from 16:20:00 UT to 16:22:00 UT) were shown in Figure 5(b) in the same format as Figure 5(a). The spectra showed a power-law distribution with an index of 4.8 between 50 and 200 keV, similar to the result in MH1.

4. Discussion and Conclusions

In this paper, we investigated two successive large spatial-scale magnetic holes in the magnetotail based on MMS

measurements. Inside both magnetic holes, the ion and electron temperature increased, the thermal pressure increased, and the magnetic pressure decreased, although the MMS crossed partially MH1 and completely MH2 as illustrated in Figure 3. It indicates that the ions and electrons were heated in these two holes. The magnetic structures of these two holes were complicated. In the core region of the MH1, an ion-scale magnetic structure was identified and thus the energetic electrons were nonadiabatic therein. Furthermore, MH1 was even varying as it was detected by the spacecraft.

There were some distinct features of these two holes. Some kinds of structural ion flows were observed inside MH1. Especially, an ion vortex was observed in the cross section of the MH1. As for the MH2, the ion flow was weak, without any structural flows. The threshold condition of the mirror-mode instability was met inside MH1 while it was not inside MH2. If these two holes were both generated by the mirror-mode instability, it suggests that they were experiencing different phases. The ions were much more dynamic inside MH1 than those inside MH2. In other words, MH2 could have evolved into the decaying phase.

One striking feature of these two holes MH1 and MH2 was the energetic electrons up to 100 keV within them, to our best knowledge, which has never been reported previously. The energetic electrons show the power-law and nonadiabatic distribution in the MH1 core region. It indicates that the electrons experienced nonadiabatic acceleration inside the hole. The evident field-aligned electrons could result from the Fermi acceleration inside the magnetic hole, similar to the observations in Yu et al. (2022). The 90° flux enhancement inside the MH1 core region could be associated with the ion-scale structure. However, it is challenging to determine the acceleration mechanism(s) inside the holes. The magnetic flux rope is another transient magnetic structure that has been widely observed in the magnetotail (Slavin et al. 2003; Zong et al. 2004; Wang et al. 2010a, 2010b, 2016b, 2016c), at the magnetopause (Russell & Elphic 1978; Wang et al. 2017b), and in the interplanetary solar wind (Wang et al. 2023a, 2023b) and other planetary magnetospheres (Zhang et al. 2012; Zhong et al. 2018; Wang et al. 2024). The energetic electrons have been detected also inside the flux ropes (Chen et al. 2008; Wang et al. 2010b). Inside the flux ropes, the electrons can be accelerated by Fermi and Betatron mechanisms while the squashed flux ropes contract (Drake et al. 2006; Fu et al. 2006; Dahlin et al. 2014; Wang et al. 2016a; Lu et al. 2018). Furthermore, the electrons can be accelerated by the reconnection electric field while the flux ropes were located inside the reconnection region (Wang et al. 2017a). These mechanisms might play a role as well while the energetic electrons are detected inside magnetic holes.

Although electron-scale vortices have been widely discussed inside the magnetic holes (Haynes et al. 2015; Roytershteyn et al. 2015), the vortices inside the magnetic holes with sizes greater than ρ_i were poorly understood. Recently, vortices with sizes greater than ρ_i but smaller than the MHD scale inside the magnetic holes were reported (Wang et al. 2021; Yao et al. 2023), which could be explained to be generated by ion diamagnetic drift. Inside our MHD scale magnetic hole, the ion frozen-in condition was satisfied (not shown) and the ion flows could be dominated by the electric drift $\frac{\boldsymbol{E} \times \boldsymbol{B}}{\boldsymbol{B}^2}$. There could not exist ion diamagnetic drift.

In conclusion, we observed energetic electrons inside two MHD scale magnetic holes in the magnetotail. Inside both magnetic holes, the spectra of energetic electrons could be power-law fitted in the energy range of 50–200 keV, which indicated that the energetic electrons were accelerated inside the magnetic holes. Meanwhile, the flux enhancement of energetic electrons in the loss cone was observed inside both magnetic holes, which indicated that energetic electrons could be trapped inside the magnetic holes. These observations suggest that MHD scale magnetic holes can still be highly dynamic.

Acknowledgments

This work is supported by the National Science Foundation of China (NSFC) grants (42174187), the key research program of frontier sciences CAS (QYZDJSSW-DQC010), National Key Research and Development Program of China (2022YFA1604600), and the Fundamental Research Funds for the Central Universities. We thank the entire MMS team and instrument principal investigators for providing and calibrating data. All the MMS data used in this work are available at the MMS data center (https://lasp.colorado.edu/mms/sdc/public/about/browse-wrapper/).

ORCID iDs

Rongsheng Wang https://orcid.org/0000-0002-9511-7660
Xinmin Li https://orcid.org/0000-0003-1553-6337
Shimou Wang https://orcid.org/0000-0002-4382-1349
Quanming Lu https://orcid.org/0000-0003-3041-2682
San Lu https://orcid.org/0000-0003-2248-5072

References

Balikhin, M. A., Sagdeev, R. Z., Walker, S. N., et al. 2009, GeoRL, 36, L03105
Blake, J. B., Mauk, B. H., Baker, D. N., et al. 2016, SSRv, 199, 309
Buchner, J., & Zelenyi, L. M. 1989, JGRA, 94, 11821
Burch, J. L., Moore, T. E., Torbert, R. B., & Giles, B. L. 2016, SSRv, 199, 5
Chen, L. J., Bhattacharjee, A., Puhl-Quinn, P. A., et al. 2008, NatPh, 4, 19
Dahlin, J. T., Drake, J. F., & Swisdak, M. 2014, PhPl, 21, 092304
Drake, J. F., Swisdak, M., Che, H., & Shay, M. A. 2006, Natur, 443, 553
Fränz, M., Burgess, D., & Horbury, T. S. 2000, JGRA, 105, 12725
Fu, X. R., Lu, Q. M., & Wang, S. 2006, PhPl, 13, 012309
Gary, S. P., & Karimabadi, H. 2006, JGRA, 111, A11224
Ge, Y. S., McFadden, J. P., Raeder, J., et al. 2011, JGRA, 116, A00I23
Haynes, C. T., Burgess, D., Camporeale, E., & Sundberg, T. 2015, PhPl, 22, 012309
Huang, S. Y., Du, J. W., Sahraoui, F., et al. 2017a, JGRA, 122, 8577
Huang, S. Y., Sahraoui, F., Yuan, Z. G., et al. 2017b, ApJL, 836, L27
Huang, S. Y., Sahraoui, F., Yuan, Z. G., et al. 2018, ApJ, 861, 29
Joy, S. P., Kivelson, M. G., Walker, R. J., et al. 2006, JGRA, 111, A12212
Liu, Y. Y., Fu, H. S., Zong, Q. G., et al. 2020, GeoRL, 47, 18
Lu, Q. M., Wang, H. Y., Huang, K., Wang, R. S., & Wang, S. 2018, PhPl, 25, 072126
Lucek, E. A., Dunlop, M. W., Balogh, A., et al. 1999, GeoRL, 26, 2159
Pokhotelov, O. A., Onishchenko, O. G., & Stenflo, L. 2013, PhyS, 87, 065303
Pollock, C., Moore, T., Jacques, A., et al. 2016, SSRv, 199, 331
Roytershteyn, V., Karimabadi, H., & Roberts, A. 2015, RSPTA, 373, 20140151
Russell, C. T., & Elphic, R. C. 1978, SSRv, 22, 681
Russell, C. T., Riedler, W., Schwingenschuh, K., & Yeroshenko, Y. 1987, GeoRL, 14, 644
Russell, C. T., Anderson, B. J., Baumjohann, W., et al. 2016, SSRv, 199, 189
Shi, Q. Q., Shen, C., Pu, Z. Y., et al. 2005, GeoRL, 32, L12105
Shi, Q. Q., Pu, Z. Y., Soucek, J., et al. 2009, JGRA, 114, A10202
Shustov, P. I., Zhang, X. J., Pritchett, P. L., et al. 2019, JGRA, 124, 342
Slavin, J. A., Lepping, R. P., Gjerloev, J., et al. 2003, JGRA, 108, 1015
Soucek, J., Lucek, E., & Dandouras, I. 2008, JGRA, 113, A04203
Southwood, D. J., & Kivelson, M. G. 1993, JGRA, 98, 9181

Sperveslage, K., Neubauer, F. M., Baumgartel, K., & Ness, N. F. 2000, NPGeo, 7, 191
Sun, W. J., Shi, Q. Q., Fu, S. Y., et al. 2012, AnGeo, 30, 583
Tsurutani, B. T., & Ho, C. M. 1999, RvGeo, 37, 517
Tsurutani, B. T., Smith, E. J., Anderson, R. R., et al. 1982, JGRA, 87, 6060
Turner, J. M., Burlaga, L. F., Ness, N. F., et al. 1977, JGR, 82, 1921
Wang, G. Q., Volwerk, M., Xiao, S. D., et al. 2022, JGRA, 127, 5
Wang, G. Q., Volwerk, M., Wu, M. Y., et al. 2021, AJ, 161, 110
Wang, H. Y., Lu, Q. M., Huang, C., & Wang, S. 2016a, ApJ, 821, 84
Wang, H. Y., Lu, Q. M., Huang, C., & Wang, S. 2017a, PhPl, 24, 052113
Wang, R. S., Lu, Q. M., Du, A. M., & Wang, S. 2010a, PhRvL, 104, 175003
Wang, R. S., Lu, Q. M., Li, X., Huang, C., & Wang, S. 2010b, JGRA, 115, A11201
Wang, R. S., Wang, S. M., Lu, Q. M., et al. 2023a, NatAs, 7, 18
Wang, R. S., Yu, X. C., Wang, Y. M., Lu, Q. M., & Lu, S. 2023b, ApJ, 947, 78
Wang, R. S., Lu, Q. M., Nakamura, R., et al. 2016b, NatPh, 12, 263
Wang, R. S., Lu, Q. M., Nakamura, R., et al. 2016c, JGRA, 121, 9473
Wang, R. S., Lu, Q. M., Nakamura, R., et al. 2017b, JGRA, 122, 10436
Wang, R. S., Cheng, Z. H., Slavin, J. A., et al. 2024, GeoRL, 51, 5
Winterhalter, D., Neugebauer, M., Goldstein, B. E., et al. 1994, JGRA, 99, 23371
Yao, S. T., Wang, X. G., Shi, Q. Q., et al. 2017, JGRA, 122, 1990
Yao, S. T., Shi, Q. Q., Yao, Z. H., et al. 2019, GeoRL, 46, 523
Yao, S. T., Shi, Q. Q., Zong, Q. G., et al. 2021, ApJ, 923, 216
Yao, S. T., Li, J. H., Zhou, X. Z., et al. 2023, JGRA, 128, 7
Yu, Y., Fu, H. S., Cao, J. B., Liu, Y. Y., & Wang, Z. 2022, ApJ, 926, 199
Zhang, T. L., Lu, Q. M., Baumjohann, W., et al. 2012, Sci, 336, 567
Zhang, X. J., Artemyev, A., Angelopoulos, V., & Horne, R. B. 2017, JGRA, 122, 10304
Zhima, Z. R., Cao, J. B., Fu, H. S., et al. 2015, JGRA, 120, 2469
Zhong, J., Wei, Y., Pu, Z. Y., et al. 2018, ApJL, 860, L20
Zhong, Z. H., Zhou, M., Huang, S. Y., et al. 2019, GeoRL, 46, 6248
Zhong, Z. H., Zhou, M., Liu, Y. H., et al. 2022, ApJL, 926, L27
Zong, Q. G., Fritz, T. A., Pu, Z. Y., et al. 2004, GeoRL, 31, L18803